



**HAL**  
open science

## **In vitro flow study in a compliant abdominal aorta phantom with a non-Newtonian blood-mimicking fluid**

Anaïs Moravia, Serge Simoëns, Mahmoud El Hajem, Benyebka Bousaïd, Pascale Kulisa, Nellie Della-Schiava, Patrick Lermusiaux

### ► To cite this version:

Anaïs Moravia, Serge Simoëns, Mahmoud El Hajem, Benyebka Bousaïd, Pascale Kulisa, et al.. In vitro flow study in a compliant abdominal aorta phantom with a non-Newtonian blood-mimicking fluid. *Journal of Biomechanics*, 2021, 130, pp.110899. 10.1016/j.jbiomech.2021.110899 . hal-03767603

**HAL Id: hal-03767603**

**<https://hal.science/hal-03767603>**

Submitted on 2 Sep 2022

**HAL** is a multi-disciplinary open access archive for the deposit and dissemination of scientific research documents, whether they are published or not. The documents may come from teaching and research institutions in France or abroad, or from public or private research centers.

L'archive ouverte pluridisciplinaire **HAL**, est destinée au dépôt et à la diffusion de documents scientifiques de niveau recherche, publiés ou non, émanant des établissements d'enseignement et de recherche français ou étrangers, des laboratoires publics ou privés.

**Title:** *In vitro* flow study in a compliant abdominal aorta phantom with a non-Newtonian blood-mimicking fluid

**Authors:** Anais Moravia<sup>a\*</sup>, Serge Simoëns<sup>a</sup>, Mahmoud El Hajem<sup>a</sup>, Benyebka Bou-Saïd<sup>b</sup>, Pascale Kulisa<sup>a</sup>, Nellie Della-Schiava<sup>c</sup>, Patrick Lermusiaux<sup>c</sup>

<sup>a</sup>*Université de Lyon, INSA de Lyon, Ecole Centrale de Lyon, Université Claude Bernard Lyon 1, CNRS, LMFA UMR 5509, Villeurbanne, France*

<sup>b</sup>*Université de Lyon, CNRS, INSA de Lyon, LaMCoS UMR5259, Villeurbanne, France*

<sup>c</sup>*Vascular and Endovascular Department, Hospices Civils de Lyon, Lyon, France*

**\* Corresponding author:**

E-mail address: [anais.moravia@ec-lyon.fr](mailto:anais.moravia@ec-lyon.fr)

Tel.: +33 6 11 45 78 39

Complete address:

INSA Lyon – LaMCoS

27 bis Avenue Jean Capelle

Bâtiment Sophie Germain

69621 Villeurbanne cedex

**Main text word count:** 3492

**Abstract (229 words)**

*In vitro* aortic flow simulators allow studying hemodynamics with a wider range of flow visualization techniques compared to *in vivo* medical imaging and without the limitations of invasive examinations. This work aims to develop an experimental bench to emulate the pulsatile circulation in a realistic aortic phantom. To mimic the blood shear thinning behavior, a non-Newtonian aqueous solution is prepared with glycerin and xanthan gum polymer. The flow is compared to a reference flow of Newtonian fluid. Particle image velocimetry is carried out to visualize 2D velocity fields in a phantom section. The experimental loop accurately recreates flowrates and pressure conditions and preserves the shear-thinning properties of the non-Newtonian fluid. Velocity profiles, shear rate, and shear stress distribution maps show that the Newtonian fluid tends to dampen the observed velocities. Preferential asymmetrical flow paths are observed in a diameter narrowing region and amplified in the non-Newtonian case. Wall shear stresses are about twice higher in the non-Newtonian case. This study shows new insights on flow patterns, velocity and shear stress distributions compared to rigid and simplified geometry aorta phantom with Newtonian fluid flows studies. The use of a non-Newtonian blood analog shows clear differences in flows compared to the Newtonian one in this compliant patient-specific geometry. The development of this aortic simulator is a promising tool to better analyze and understand aortic hemodynamics and to aid in clinical decision-making.

**Keywords:** aorta; circulatory mock loop; PIV; blood-mimicking fluid; non-Newtonian

## 1 **1. Introduction (3492 words)**

2 Over the past decade, aorta hemodynamics studies have grown considerably with the purpose not only of improving  
3 treatments but also of preventing disease by understanding their development mechanisms. Vortical flows, wall shear  
4 stresses, and modification of vessel wall mechanical properties are among the main factors that could explain the  
5 results of aortic diseases such as aneurysm and aortic dissection (Bürk et al., 2012, Kolipaka et al., 2017). *In vivo*,  
6 these characteristic investigations have shown some limitations regarding invasive measurement methods, and  
7 insufficient spatial and temporal resolutions of medical imaging techniques. To overcome these limitations *in vitro*  
8 and *in silico* approaches were developed to recreate hemodynamical environments while controlling physiological  
9 conditions, circulating fluid, and aorta material properties. *In vitro* studies allow the use of high-resolution flow  
10 visualization techniques with fewer restrictions than invasive measurement probes and the ability to conduct  
11 reproducible experiments. Particle Image Velocimetry (PIV) (Deplano et al., 2016; Najjari et al., 2016b; Büsen et al.,  
12 2017), and 3D-Particle Tracking Velocimetry (Gülan et al., 2012) have been used in hemodynamics studies to provide  
13 high spatial resolution (under  $1 \times 1 \text{ mm}^2$ ) to complement *in vivo* observations.

14 In the case of blood flow *in vitro* simulators, the main difficulty is to recreate aortic flows with complex features:  
15 realistic aorta geometry, aortic wall compliance (Deplano et al., 2007), blood non-Newtonian behavior (Deplano et  
16 al., 2014; Walker et al. 2014), and faithful pulsatile flow conditions (Thirugnanasambandam et al., 2021). Each of  
17 these characteristics plays a major role in hemodynamical flows. The challenge lies in combining them in a single  
18 experiment.

19 Many circulatory mock loops have been designed to emulate human circulation (Kung et al. 2011;  
20 Thirugnanasambandam et al., 2021) and recent research mainly focuses on improving biofidelity of *in vitro* simulators  
21 with patient custom features. Franzetti et al. (2019) and Bonfanti et al. (2020) developed an *in vitro* circulatory mock  
22 loop for aortic dissection investigations and compared it to numerical simulations. Their aorta geometry was extracted  
23 from Computed Tomography scans (CT) and custom Windkessel models were implemented to meet the patient's *in*  
24 *vivo* conditions. In addition, their aorta phantom was a rigid model and the working fluid was a Newtonian blood  
25 analog.

26 A large majority of *in vitro* (and *in silico*) studies used a Newtonian representation for blood and did not consider  
27 the shear-thinning behavior (Yousif et al., 2011; Büsen et al., 2017) claiming that blood Newtonian assumption is  
28 acceptable in large vessels such the aorta. Deplano et al. (2014) analyzed the influence of shear-thinning properties  
29 on vortex rings propagation in an idealized model of aortic aneurysm. They showed that the Newtonian fluid tends to  
30 overestimate vortex ring velocity and travel distance compared to the shear-thinning case. Non-Newtonian blood  
31 analogs are therefore, more reliable to realistically mimic aortic hemodynamical flows, at least in certain specific  
32 geometries and conditions.

33 *In vitro* studies with non-Newtonian blood analog are emerging but most of them are conducted on idealized and  
34 rigid models such as curved channels (Najjari et al., 2016b) representing the aortic arch or straight partially occluded  
35 tubes for stenosed arteries (Walker et al., 2014). Realistic aorta models with compliant walls are still lacking while  
36 these features could make the difference in biofidelity. This lack is mainly due to the difficulties in manufacturing  
37 such models when considering geometry complexity, material waterproof, need for transparency for optical  
38 techniques, and mechanical properties (Yazdi et al., 2018). Usable materials and manufacturing options are limited to  
39 some silicone molding techniques (Hütter et al., 2016; Büsen et al., 2017) and a few 3D printing resins.

40 To the authors knowledge, no study has combined *in vitro* pulsatile flow mock loop, patient-specific aorta phantom,  
41 compliant walls, and non-Newtonian blood mimicking fluid (table A1, appendix). Some of the previously cited studies  
42 investigated the impact of experimental features simplification and showed the necessity of realistic geometries and  
43 fluid-wall interactions brought by the compliance (Deplano et al., 2007; Perktold et al. 1994, Zimmermann et al.  
44 2021). The non-Newtonian fluid necessity is however more controversial as contradictory results emerged from  
45 different studies (Deplano et al., 2014; Bonfanti et al., 2020). To address these shortcomings, a circulatory mock loop  
46 was designed to mimic aortic pulsatile flows in a compliant aorta phantom with anatomically accurate geometry. A  
47 blood mimicking fluid with shear-thinning properties was used to replicate blood viscosity. It was compared with a  
48 reference Newtonian blood analog. Flow velocity fields were assessed with PIV technique for different cardiac cycle  
49 instants. Analyses of velocity profiles, shear rate, and shear stress distributions highlight the differences between  
50 Newtonian and non-Newtonian fluids in an aortic region with slight diameter variation (14.4% narrowing).

## 2. Methods

### 2.1. Aorta phantom

The aorta phantom, supplied by Segula Technologies (France), was molded out of transparent silicone. The geometry was extracted from a patient CT scan provided by Hospices Civils de Lyon. The 3D reconstitution was achieved with the software Simpleware ScanIP (Synopsis) and was simplified to only replicate the abdominal aorta and the iliac arteries. Other main aorta branches were excluded from the model. The phantom had compliant walls with a wall thickness of  $2 \pm 0.42$  mm and an elastic modulus of 0.53 MPa. The modulus was consistent with the range of human aorta elasticities from 0.25 MPa to 1.7 MPa on healthy patients (Lang et al. 1994).

### 2.2. Blood Mimicking Fluids (BMF)

Blood's non-Newtonian behavior is brought up by its shear-thinning viscosity which is related to aggregations and deformations properties of red blood cells (Baskurt et al., 2003). Mixtures of water, glycerol, and xanthan gum polymer allow mimicking human blood shear-thinning behavior while maintaining an optically clear fluid (Deplano et al., 2014; Najjari et al., 2016a), an essential property when implementing optical methods. Moreover, refractive index (RI) correction can be achieved with salts such as NaCl, KSCN, or NaI (Yousif et al., 2011; Najjari et al., 2016a) to match the phantom RI (about 1.400), and thus minimize optical distortions. The current BMF was designed to match both human blood viscosity with 45% hematocrit (at a physiological temperature of 37°C) and aorta phantom RI at the experimental working temperature of 25°C.

To characterize the viscosity of the fluids, a MCR-302 rheometer with a cone plate geometry was used. The protocol consisted in measuring each fluid's viscosity under a descending logarithmic shear-rate sweep from 1000 down to  $0.01 \text{ s}^{-1}$  at constant temperature ( $T = 25 \pm 0.01 \text{ }^\circ\text{C}$ ). An aqueous solution of 37.6% (by weight), glycerin 7.4% (by weight) NaCl, and 200 ppm xanthan gum was selected to serve as non-Newtonian BMF. A Newtonian reference fluid was obtained with an aqueous solution of 37.6% (by weight) glycerin, and NaCl 7.4% (by weight). Both fluids had a density of  $1146 \text{ kg}\cdot\text{m}^{-3}$  and  $\text{RI} = 1.399$ . Figure 1 shows the viscosities of the non-Newtonian BMF and the Newtonian reference fluid. A comparison with human blood viscosities from Thurston (1979) and Chien (1970) is

76 also provided in this graph. For the non-Newtonian BMF, apparent viscosity (at high shear rate) was  $\mu_{\infty} = 5.2$  mPa.s  
77 and the Newtonian fluid exhibited a constant viscosity of  $\mu_{\text{newt}} = 3.9$  mPa.s. The fluid sensitivity to working  
78 temperature was evaluated within a range of  $25 \pm 2$  °C. Viscosity measurements showed no differences in the range  
79 of studied shear rates (not shown here).

### 81 2.3. Experimental set-up

82 The experimental loop was designed to recreate (i) pulsatile flowrate and pressure conditions in the arterial circulation,  
83 (ii) ensure cycle reproducibility, (iii) preserve the fluid shear-thinning properties, and (iv) provide optical access for  
84 PIV measurements. A CompactRIO 9035 real-time operation controller from National Instrument was implemented  
85 and driven using a LabVIEW program to monitor pulsatile flows while ensuring cycle synchronization with the PIV  
86 system.

87 The main loop consisted of a reservoir containing the BMF, a pump, a Posiflow proportional solenoid valve  
88 (ASCO) controlling the pulsatile flow, and the aorta phantom (figure 2a.). Inlet and outlet magnetic flowmeters  
89 (Rosemount 8700, Emerson) and pressure sensors (PN 2298, IFM) monitored flows with a time resolution of 20 ms.  
90 Upstream from the solenoid valve, a bypass loop redirected the extra flow to the reservoir. This bypass prevented  
91 pump instabilities when the solenoid valve was closing during the diastolic phase. The aorta phantom was immersed  
92 in a rectangular plexiglass tank filled up with the Newtonian reference fluid (RI = 1.399). This configuration  
93 minimized optical distortions when imaging particles in the aorta phantom.

94 At each iliac artery exit, peripheral vessel resistances were represented by ball valves. Unlike rigid phantom  
95 experiments (Deplano et al., 2006, Walker et al., 2014, Franzetti et al., 2021), the phantom flexible walls ensured the  
96 compliant nature of the system with no need for an extra compliance chamber to dampen inflow conditions.

97 Xanthan gum is sensitive to shear which risks breaking its polymer chains. This process affects the shear-  
98 thinning properties of the solution. Xanthan can be damaged by commonly used pumping systems such as gear or  
99 piston pumps. Deplano et al. (2014) addressed this issue by controlling the contractile motion of an artificial ventricle  
100 to push the BMF in the main loop. In the present study, the use of a progressive cavity pump (Eco-Moineau-C, PCM)

101 allowed to minimize shear on the working fluid and prevent breaking polymer chains. The fluid viscosity properties  
102 were measured and appeared constant during the experiments (figure B1, appendix).

103 The solenoid valve was programmed to recreate flowrates waveform from Cheng et al. 2003 (MRI data in  
104 the infrarenal region on human subjects under resting conditions). The mean and maximum inlet flowrates were equal  
105 to  $Q_{\text{mean}} = 1.70 \text{ L/min}$  and  $Q_{\text{max}} = 5.80 \text{ L/min}$  respectively. The cycle period was set to  $T = 0.800 \text{ s}$ . Outlet pressure  
106 varied between 90 and 135 mmHg during a cardiac cycle.

#### 107 2.4. PIV measurements

109 Particle Image Velocimetry (PIV) technique was implemented to acquire velocity fields of the aorta phantom flow.  
110 The region of interest (ROI) was a lateral plane in the abdominal aorta (figure 2b.). It included a local diameter  
111 narrowing section. The fluid was seeded with 20-50  $\mu\text{m}$  fluorescent particles (PMMA-RhB,  $d = 1190 \text{ kg}\cdot\text{m}^{-3}$ ,  
112 LaVision, Germany). They were illuminated by a 1 mm thick laser sheet emitted by a double-pulsed Nd:YAG laser  
113 (nanoPIV,  $\lambda = 532 \text{ nm}$ , Litron laser). An Imager sCMOS camera (2560 x 2160 pixels, LaVision) was equipped with  
114 a 60 mm lens and synchronized with the laser pulses to capture pairs of images with a time interval  $\Delta t$ . Flow velocity  
115 strongly varied along the cardiac cycle. The interval  $\Delta t$  was adapted to the imaged cycle instant to ensure consistent  
116 particle displacement between each pair of images (figure 3). The PIV imaging triggers are synchronized with the  
117 solenoid valve control to make sure images are shot at the targeted instant in cycle.

#### 119 2.5. Image -processing

121 Firstly, image post-processing consisted in detecting the phantom compliant wall positions for each cycle instant with  
122 a MATLAB custom program. Walls were detected and tracked with threshold and morphological closing algorithms.  
123 Data were then averaged on the 500 images of each cycle instants. This script provided aorta diameter variations in  
124 the ROI and masking images for cross-correlation analysis to obtain vector fields (figure B2, appendix).

125 Particle images were then processed with Davis 10 software (LaVision) to compute vector fields. Images  
126 were masked out with the pre-computed masks to deactivate non-interesting pixels: background and vessel wall.  
127 Image cross-correlation was performed with a multipass method on the non-masked area limited to the aorta lumen.

128 The first path was achieved with 64x64 pixels interrogation windows with an ellipsoid weight (long axis in the flow  
129 main direction x). The second and third paths consisted of 32x32 pixels interrogation windows with a round gaussian  
130 weight and 75% overlap. For each field, missing vectors (less than 1% of computed vectors) were filled up with a  
131 polynomial interpolation algorithm and a 3x3 smoothing filter was applied. The final resolution of vector fields was  
132 0.95x0.95 mm<sup>2</sup> (about 0.6% of the aorta cross-sectional area in the ROI) and velocity uncertainties are provided in  
133 table 1. 400 images are needed to reach velocity field statistical convergence in the worst case scenario (figure B3,  
134 appendix).

135 Finally, vector field post-processing was performed with a custom MATLAB script to compute and analyze  
136 quantities of interest.

### 138 3. Results

#### 139 3.1. Flow and wall displacement characteristics

140 Flow conditions control comparison was achieved between the Newtonian and non-Newtonian experiments with a  
141 consistent match between flowrates, pressure, peak Reynolds ( $Re_{peak} = \rho D_{peak} V_{peak} / \mu$ ) and Womersley ( $\alpha =$   
142  $D\sqrt{\omega\rho/\mu}$ ) numbers (table 2).  $D_{peak}$  and  $V_{peak}$  are the mean aorta diameter and velocity at the systolic peak,  $D$  is the  
143 aorta mean diameter along a cycle, and  $\omega = \frac{1}{T}$  is the pulse period. The cycle-to-cycle mean and standard deviation  
144 quantities were calculated over the 6000 cycles recorded along the PIV measurements (figure 2c. and figure B4 in the  
145 appendix). Note that the flowmeters only integrated positive flowrates which do not allow to visualize the backflow  
146 and diastolic phases. The aortic wall compliance generated backflows that were observed on the PIV images but not  
147 with the inlet flowmeter. Therefore, aorta ROI flowrate was estimated with PIV measurements, the aorta diameter  
148 variations along the cycle, and the hypothesis of a circular cross-section (figure 3). The systole magnitude was  
149 consistent with inlet flowmeter measurements (figure 2c.).

150 Table 3 shows both fluid experiment wall displacement characteristics. According to Sonesson et al., 1994, the  
151 observed range of diameter changes ( $0.92 \pm 0.099$  mm for the Newtonian and  $1.2 \pm 0.15$  mm for the non-Newtonian  
152 experiment) are consistent with a 53 - 69 years old male patient.

153

154 

### 3.2. Velocity profiles and maps

155 Velocity profiles for the Newtonian and non-Newtonian BMF are presented in figure 4 at 4 distinct cycle instants  
 156 numbered with k indexes (k = 2, 4, 6, 10): near systolic peak, systole deceleration, backflow transition, and diastole.  
 157 Velocity profiles were drawn for three locations (a,b,c) of the aorta phantom (figure 4). Both flows exhibited the same  
 158 velocity trends with a strong asymmetry. The non-Newtonian fluid flow showed higher velocity extrema. To evaluate  
 159 the mean difference between the two profiles, a normalized root mean square error was calculated with equation 1.

$$160 \quad NRMSE = \frac{\sqrt{\sum_{i=1}^N (u_{x,i}^{newt} - u_{x,i}^{non\ newt})^2}}{\sum_{i=1}^N \left( \frac{u_{x,i}^{newt} + u_{x,i}^{non\ newt}}{2} \right)} \quad (1)$$

161 with  $u_{x,i}^{newt}$  and  $u_{x,i}^{non\ newt}$  Newtonian and non-Newtonian velocity profiles respectively. N is the number of points on  
 162 the profile line (N = 100). This error was normalized by the mean velocity between Newtonian and non-Newtonian  
 163 profiles at a specific instant k. Note that the observed difference exceeded the uncertainty of velocity maps provided  
 164 in table 1. The velocity difference was particularly high at the diastolic phase (up to 199% difference) where a flatter  
 165 profile was observed for the Newtonian case. Velocity maps were computed for the same 4 cycle instants (figure 5).  
 166 A high-velocity path was observed at k = 2 and k = 4 for both fluid flows. This preferred trajectory seemed to be  
 167 directed by the curvature of the aorta upper wall (y/D = D on profiles) with a narrowing in diameter (path arrow on  
 168 maps figure 5). Backflow was observed on k = 6 and seemed to oppose this high-velocity path resulting in a low axial  
 169 velocity region. At post-systole (k = 6 and k = 10), a preferred backflow path arose along the lower wall in figure 5  
 170 (y/D = 0 on profiles figure 4). Moreover, swirling structures appeared near the top wall. During diastole, these  
 171 structures were pushed down by the higher velocity path for the non-Newtonian fluid while their displacement was  
 172 limited in the Newtonian case.

173

174 

### 3.3. Shear rate and shear stress distribution

175 It appeared that due to the aorta geometry, certain preferential flow paths were amplified in the non-Newtonian case.  
 176 To investigate these path consequences, the shear rate was calculated (equation 2) and is shown in figure 6a.

$$\dot{\gamma} = \frac{\partial u_y}{\partial x} + \frac{\partial u_x}{\partial y} \quad (2)$$

For the non-Newtonian fluid, corresponding viscosity maps were computed with shear rate dependent viscosity  $\mu(\dot{\gamma}_{norm})$  data from the rheology study (figure 1) and the shear-rate  $\dot{\gamma}_{norm}$  from equation 3. Shear stress was then calculated with equation 4 (figure 6b). In the Newtonian case, viscosity was a constant  $\mu(\dot{\gamma}_{norm}) = \mu_{newt} = 3.9$  mPa.s.

$$\dot{\gamma}_{norm} = \sqrt{\frac{\partial u_y^2}{\partial x} + \frac{\partial u_x^2}{\partial y}} \quad (3)$$

$$T_{ss} = \mu(\dot{\gamma}_{norm}) \cdot \dot{\gamma} \quad (4)$$

The shear stress is plotted for the 12 cycle instants (figure 7). Mean shear stress (integration on the whole ROI) and wall shear stress ( $T_{wss}$ ) are presented as absolute terms. A  $T_{wss}$  per instants was evaluated as a mean shear stress  $\mu(\dot{\gamma}_{norm}) \cdot \frac{\partial u}{\partial y}$  on a near-wall layer (5% of aorta diameter thick layer along the upper and lower walls). On the whole ROI, shear stress was about three times higher for the non-Newtonian fluid than for Newtonian fluid.  $|T_{wss}|$  was twice higher for the non-Newtonian BMF with a maximum and average shear stress of 0.23 Pa and 0.071 Pa respectively while they were of 0.11 Pa and 0.035 Pa for the Newtonian fluid. Since the non-Newtonian fluid equivalent viscosity (at high shear rate) was 33.3% higher than the Newtonian fluid one, global higher shear stress values were expected. However, the 200% increase and shear distribution discrepancies in the ROI could not be attributed to this shift in overall viscosity.

## 4. Discussion

### 4.1. Related geometry flow distribution

The analysis mainly focused on the four previously described instants which represent very distinct cardiac cycle phases (systolic peak, deceleration, backflow, and diastole). One of the main observations on velocity field maps was the upper wall flow jet-like deviation in the narrowed region at systole. Recirculation paths appeared on the opposite wall at diastole. These flow patterns were observed in Wittberg et al. (2016) where aorta geometry irregularities influence on flow were studied with numerical simulation on a non-Newtonian blood flow. A local reduction of the

201 diameter induces a deflected flow jet in the curvature direction which persisted downstream of the narrowing. These  
202 results also showed chaotic flow, vortical motions, and higher wall shear stress around the section narrowing. In the  
203 current study, this effect was amplified for the non-Newtonian case. Hun et al. (2004) and Neofytou (2006) studied  
204 the development of asymmetric flows that were specific for non-Newtonian fluid flows. They showed that these  
205 asymmetries appeared downstream from the singularities and were amplified when Reynolds number increases  
206 ( $>500$ ). Moreover, Amornsamankul et al. (2007) investigated the influence of non-Newtonian fluid characteristics  
207 on flow patterns in symmetric and asymmetric tube geometries and highlighted similar velocity profiles when  
208 comparing Newtonian and non-Newtonian fluids. In our non-Newtonian experiment, the maximum Reynolds number  
209 at systole was  $Re_{\text{peak}} = 1129$  which could explain the amplified asymmetry in the aorta ROI. Shear stress  
210 Measured  $T_{\text{WSS}}$  remained in the lower range of in vivo measurements in healthy aortas in the non-Newtonian case  
211 (Kolipaka et al., 2017; Cheng et al., 2003). Note that PIV images resolution and the missing velocity third dimension  
212 component tend to underestimate velocity gradients (Tokgoz et al., 2012). Therefore, the calculated shear stresses  
213 give clues on distribution and evolution along the cycle but cannot be directly compared with *in vivo* absolute values.  
214 Many numerical studies were conducted on smaller arterial systems (femoral, coronary, etc) and showed that  
215 Newtonian representations underestimate WSS compared to non-Newtonian models (Apostolidis et al., 2016;  
216 Weddell et al., 2015). Numerous studies on large arteries showed that the Newtonian assumption is acceptable  
217 (Caballero et al., 2015; Iasiello et al., 2017) but most of them were conducted on simplified and idealized geometries.  
218 The previous observations on increased flow asymmetry for non-Newtonian fluid came with higher shear stress values  
219 and different patterns while inflow conditions and measurings methods were similar. These results question the  
220 Newtonian assumption at least in a more complex geometry with compliant walls.

#### 222 4.2. Limitations

223 The non-Newtonian working fluid was designed to approach human blood shear-thinning viscosity. Human blood  
224 reaches a viscosity plateau at low shear rates. The designed BMF did not reach this plateau and thus, did not well  
225 mimic human blood in this lower range of shear rate. It would result in an overestimation of viscosity at low shear  
226 rate ( $<0.01$  mPa.s) which could question shear stress results. Moreover, other rheological properties such as

viscoelasticity were not explored in our xanthan solution (Campo-Deaño et al., 2013; Najjari et al., 2016a). Brookshier and Tarbell (1993) showed that xanthan gum was a good candidate to mimic blood viscoelasticity compared to other polymers. In this study, more complex rheometric devices are needed to explore low shear rates and viscoelasticity (oscillatory and capillary rheometers). In addition, a 3D visualization technique (slices of stereo-PIV) could provide information on the 3<sup>rd</sup> dimension to better estimate velocity gradients and thus wall shear stress.

## **5. Conclusion**

The developed aortic flow simulator emulated reproducible flowrate and pressure conditions on an anatomically realistic compliant aorta phantom with non-Newtonian blood mimicking fluid. Particle image velocimetry provided high-resolution flow visualizations on a phantom 2D plane to compute quantities of interest such as shear rate, viscosity, and shear stress distributions. The use of a non-Newtonian BMF strongly influenced flow and shear rate distributions in this complex geometry model of the aorta. Further analyses have to be conducted on the development of vortical structure, turbulence, and 3D flow distributions. The adaptable set-up was designed to accommodate different flow visualization techniques (Stereo-PIV and 3D-PTV), different types of vessel phantom geometry (aneurysm and aortic dissection), and customizable inflow conditions. This simulator is a promising tool to study hemodynamics in healthy and pathological vessels and more fundamental flow investigations.

## **Conflict of interest**

All authors declare that they have no conflicts of interest.

## **Acknowledgements**

This project is granted by AURA region under the label Pack ambition 2018 @NEDA (18001168001).

250 **References**

- 251 Amornsamankul, S., Wiwatanapataphee, B., Wu, Y. H., & Lenbury, Y., 2006. Effect of non-Newtonian behaviour of  
252 blood on pulsatile flows in stenotic arteries. *International Journal of Biological and Medical Sciences*, 1(1), 42-  
253 46.
- 254 Anastasiou, A. D., Spyrogianni, A. S., Koskinas, K. C., Giannoglou, G. D., & Paras, S. V., 2012. Experimental  
255 investigation of the flow of a blood analogue fluid in a replica of a bifurcated small artery. *Medical engineering  
256 & physics*, 34(2), 211-218.
- 257 Apostolidis, A. J., Moyer, A. P., Beris, A. N., 2016. Non-Newtonian effects in simulations of coronary arterial blood  
258 flow. *Journal of Non-Newtonian Fluid Mechanics*, 233, 155-165.
- 259 Baskurt, O. K., Meiselman, H. J., 2003. Blood rheology and hemodynamics. In: *Seminars in thrombosis and  
260 hemostasis* 29(5), 435-450.
- 261 Bonfanti, M., Franzetti, G., Homer-Vanniasinkam, S., Díaz-Zuccarini, V., Balabani, S., 2020. A Combined In Vivo,  
262 In Vitro, In Silico Approach for Patient-Specific Haemodynamic Studies of Aortic Dissection. *Annals of  
263 Biomedical Engineering*, 48(12), 2950-2964.
- 264 Brookshier, K.A. Tarbell J.M., 1993. Evaluation of a transparent blood analog fluid: aqueous xanthan gum/glycerine  
265 Biorheology, 30, 107-116
- 266 Bürk, J., Blanke, P., Stankovic, Z., Barker, A., Russe, M., Geiger, J., Frydrychowicz, A., Markl, M., 2012. Evaluation  
267 of 3D blood flow patterns and wall shear stress in the normal and dilated thoracic aorta using flow-sensitive 4D  
268 CMR. *Journal of cardiovascular magnetic resonance*, 14(1), 1-11.
- 269 Büsen, M., Arenz, C., Neidlin, M., Liao, S., Schmitz-Rode, T., Steinseifer, U., Sonntag, S. J., 2017. Development of  
270 an in vitro PIV setup for preliminary investigation of the effects of aortic compliance on flow patterns and  
271 hemodynamics. *Cardiovascular engineering and technology*, 8(3), 368-377.
- 272 Caballero, A. D., Laín, S., 2015. Numerical simulation of non-Newtonian blood flow dynamics in human thoracic  
273 aorta. *Computer methods in biomechanics and biomedical engineering*, 18(11), 1200-1216.

274 Campo-Deaño L, Dullens RP, Aarts DG, Pinho FT, Oliveira MS., 2013. Viscoelasticity of blood and viscoelastic blood  
275 analogues for use in polydimethylsiloxane in vitro models of the circulatory system. *Biomicrofluidics.*,  
276 7(3),034102.

277 Cheng, C. P., Herfkens, R. J., Taylor, C. A., 2003. Comparison of abdominal aortic hemodynamics between men and  
278 women at rest and during lower limb exercise. *Journal of vascular surgery*, 37(1), 118-123.

279 Chien, S., 1970. Shear dependence of effective cell volume as a determinant of blood viscosity. *Science*, 168(3934),  
280 977-979

281 Deplano, V., Knapp, Y., Bertrand, E., Gaillard, E., 2007. Flow behaviour in an asymmetric compliant experimental  
282 model for abdominal aortic aneurysm. *Journal of biomechanics*, 40(11), 2406-2413.

283 Deplano, V., Knapp, Y., Bailly, L., Bertrand, E., 2014. Flow of a blood analogue fluid in a compliant abdominal aortic  
284 aneurysm model: Experimental modelling. *Journal of biomechanics*, 47(6), 1262-1269.

285 Deplano, V., Guivier-Curien, C., Bertrand, E., 2016. 3D analysis of vortical structures in an abdominal aortic aneurysm  
286 by stereoscopic PIV. *Experiments in Fluids*, 57(11), 1-11.

287 Franzetti, G., Diaz-Zuccarini, V., & Balabani, S., 2019. Design of an In Vitro Mock Circulatory Loop to Reproduce  
288 Patient-Specific Vascular Conditions: Toward Precision Medicine. *Journal of Engineering and Science in Medical  
289 Diagnostics and Therapy*, 2(4), 041004.

290 Gijssen, F. J., van de Vosse, F. N., & Janssen, J. D., 1999. The influence of the non-Newtonian properties of blood on  
291 the flow in large arteries: steady flow in a carotid bifurcation model. *Journal of biomechanics*, 32(6), 601-608.

292 Gülan, U., Lüthi, B., Holzner, M., Liberzon, A., Tsinober, A., Kinzelbach, W., 2012. Experimental study of aortic flow  
293 in the ascending aorta via particle tracking velocimetry. *Experiments in fluids*, 53(5), 1469-1485.

294 Hun, J., Park, J. W., Park, C. G., 2004. Asymmetric flows of non-Newtonian fluids in symmetric stenosed artery.  
295 *Korea-Australia Rheology Journal*, 16(2), 101-108.

296 Hütter, L., Geoghegan, P. H., Docherty, P. D., Lazarjan, M. S., Clucas, D., Jermy, M., 2016. Fabrication of a compliant  
297 phantom of the human aortic arch for use in Particle Image Velocimetry (PIV) experimentation. *Current  
298 Directions in Biomedical Engineering*, 2(1), 493-497.

299 Iasiello, M., Vafai, K., Andreozzi, A., Bianco, N., 2017. Analysis of non-Newtonian effects within an aorta-iliac  
300 bifurcation region. *Journal of biomechanics*, 64, 153-163.

301 Jcgm, J. C. G. M., 2008. Evaluation of measurement data—Guide to the expression of uncertainty in measurement.  
302 Int. Organ. Stand. Geneva ISBN, 50, 134.

303 Kolipaka, A., Illapani, V. S. P., Kalra, P., Garcia, J., Mo, X., Markl, M., & White, R. D., 2017. Quantification and  
304 comparison of 4D flow MRI derived wall shear stress and MRE derived wall stiffness of the abdominal aorta.  
305 Journal of Magnetic Resonance Imaging, 45(3), 771-778.

306 Kung, E. O., Taylor, C. A., 2011. Development of a physical Windkessel module to re-create in vivo vascular flow  
307 impedance for in vitro experiments. Cardiovascular engineering and technology, 2(1), 2-14.

308 Lang, R. M., Cholley, B. P., Korcarz, C., Marcus, R. H., Shroff, S. G., 1994. Measurement of regional elastic properties  
309 of the human aorta. A new application of transesophageal echocardiography with automated border detection and  
310 calibrated subclavian pulse tracings. Circulation, 90(4), 1875-1882.

311 Najjari, M. R., Hinke, J. A., Bulusu, K. V., & Plesniak, M. W., 2016. On the rheology of refractive-index-matched,  
312 non-Newtonian blood-analog fluids for PIV experiments. Experiments in Fluids, 57(6), 96.

313 Najjari, M. R., & Plesniak, M. W., 2016. Evolution of vortical structures in a curved artery model with non-Newtonian  
314 blood-analog fluid under pulsatile inflow conditions. Experiments in Fluids, 57(6), 1-16.

315 Najjari, M. R., & Plesniak, M. W., 2018. Secondary flow vortical structures in a 180° elastic curved vessel with torsion  
316 under steady and pulsatile inflow conditions. Physical Review Fluids, 3(1), 013101.

317 Neofytou, P., 2006. Transition to asymmetry of generalised Newtonian fluid flows through a symmetric sudden  
318 expansion. Journal of Non-Newtonian Fluid Mechanics, 133. 132-140

319 Perktold, K., Thurner, E., & Kenner, T., 1994. Flow and stress characteristics in rigid walled and compliant carotid  
320 artery bifurcation models. Medical & biological engineering & computing, 32(1), 19-26.

321 Schirmer, C. M., & Malek, A. M., 2007. Wall shear stress gradient analysis within an idealized stenosis using non-  
322 Newtonian flow. Neurosurgery, 61(4), 853-864.

323 Sonesson, B., Länne, T., Vernersson, E., & Hansen, F., 1994. Sex difference in the mechanical properties of the  
324 abdominal aorta in human beings. Journal of vascular surgery, 20(6), 959-969.

325 Stamatopoulos, C., Mathioulakis, D. S., Papaharilaou, Y., & Katsamouris, A., 2011. Experimental unsteady flow study  
326 in a patient-specific abdominal aortic aneurysm model. Experiments in fluids, 50(6), 1695-1709.

327 Tokgoz, S., Elsinga, G. E., Delfos, R., & Westerweel, J., 2012. Spatial resolution and dissipation rate estimation in  
328 Taylor--Couette flow for tomographic PIV. *Experiments in fluids*, 53(3), 561-583.

329 Thurston, G. B., 1979. Rheological parameters for the viscosity viscoelasticity and thixotropy of blood. *Biorheology*,  
330 16(3), 149-162.

331 Thirugnanasambandam, M., Canchi, T., Piskin, S., Karmonik, C., Kung, E., Menon, P. G., Avril, S., Finol, E. A.  
332 (2021). Design, Development, and Temporal Evaluation of a Magnetic Resonance Imaging-Compatible In Vitro  
333 Circulation Model Using a Compliant Abdominal Aortic Aneurysm Phantom. *Journal of Biomechanical*  
334 *Engineering*, 143(5), 051004.

335 Walker, A. M., Johnston, C. R., Rival, D. E., 2014. On the characterization of a non-Newtonian blood analog and its  
336 response to pulsatile flow downstream of a simplified stenosis. *Annals of biomedical engineering*, 42(1), 97-109.

337 Weddell, J. C., Kwack, J., Imoukhuede, P. I., Masud, A., 2015. Hemodynamic analysis in an idealized artery tree:  
338 differences in wall shear stress between Newtonian and non-Newtonian blood models. *PloS one*, 10(4),  
339 e0124575.

340 Wittberg, L. P., van Wyk, S., Fuchs, L., Gutmark, E., Backeljauw, P., Gutmark-Little, I., 2016. Effects of aortic  
341 irregularities on blood flow. *Biomechanics and modeling in mechanobiology*, 15(2), 345-360.

342 Yazdi, S. G., Geoghegan, P. H., Docherty, P. D., Jermy, M., Khanafer, A., 2018. A review of arterial phantom  
343 fabrication methods for flow measurement using PIV techniques. *Annals of biomedical engineering*, 46(11),  
344 1697-1721.

345 Yousif, M. Y., Holdsworth, D. W., Poepping, T. L., 2011. A blood-mimicking fluid for particle image velocimetry with  
346 silicone vascular models. *Experiments in fluids*, 50(3), 769-774.

347 Zimmermann, J., Loecher, M., Kolawole, F. O., Bäuml, K., Gifford, K., Dual, S. A., ... & Ennis, D. B., 2021. On  
348 the impact of vessel wall stiffness on quantitative flow dynamics in a synthetic model of the thoracic aorta.  
349 *Scientific Reports*, 11(1), 1-14.

## **Figure legends**

Figure 1: Measurement of dynamic viscosity as a function of shear rate for the Newtonian and non-Newtonian fluids. Comparison with reference human blood data from Thurston (1979) and Chien (1970).

Figure 2: (a) Illustration of the experimental setup with the circulatory mock loop, PIV equipment, and aorta phantom immersed in the tank. (b) CAD model of the aorta phantom biofidelic geometry showing the imaged plane with PIV and the region of interest (ROI), (c) flowrate and pressure waveforms along two successive cardiac cycles. Solid and dashed lines represent mean cycles on the 12 x 500 generated cycles and shaded areas represent standard deviation.

Figure 3: The curve is an estimation of flowrate in the aorta ROI from PIV velocity fields and aorta diameter. The circles correspond to recorded instants with PIV images. A number of 500 images were used per cycle instant to calculate flowrate.. The corresponding table shows data acquisition program for the PIV experiments. At each cardiac cycle, 500 pairs of images are shot during 500 successive cycles. Therefore, a total of 6000 successive cycles (12 x 500) were needed to capture the 500 images of each of the 12 targeted instants.

Figure 4: Velocity profiles for the Newtonian and non-Newtonian fluids at three locations of the aorta ROI. Corresponding instants are drawn on the flowrate curve where the circles correspond to recorded instants with PIV images.. Normalized root mean square error from eq. (A) is indicated at the bottom right side of each profile. Each velocity profile is computed on 500 PIV images shot at the same instant.

Figure 5: Velocity maps for the Newtonian (left) and non-Newtonian (right) fluids at four cycles instants ( $k = 2, 4, 6$  and 10). Each instant map is a mean velocity field from the 500 PIV images for the corresponding instant.

Figure 6: (a) Shear-rate maps for the Newtonian and non-Newtonian fluids at four cycle instants  $k = 2, 4, 6,$  and 10, (b) shear stress for the Newtonian and non-Newtonian fluids at 4 cycle instants  $k = 2, 4, 6,$  and 10. The colormap covered a narrower range for the Newtonian fluid.

Figure 7: (left) Shear stress absolute term calculated on the aorta ROI versus time, (right) Wall shear stress on a 5% of aorta diameter thick layer along upper and lower walls versus time.

## **Table legends**

Table 1: Mean and maximum uncertainties computed on the whole set of PIV images. Maximum error corresponds to the worst case error in the interrogation windows. For each cycle instant, the error was computed with the Type A uncertainty method (JCGM, 2008) for all the interrogation windows of the 12 velocity fields ( $n = 500$  data for each field). The mean error is the mean uncertainty on of all the interrogation windows of the 12 cycle instants. The maximum error is the worst uncertainty found in an interrogation window.

Table 2: Newtonian and non-Newtonian flow experiments parameters. Reynolds and Womersley numbers were calculated with equivalent viscosity at high shear rate for the non-Newtonian case. The peak Reynolds number was calculated with systolic peak diameter and velocity data. Data are provided with their standard deviations computed over the 6000 cycles.

Table 3: Diameter change with mean and standard deviation values based on diameter computation with PIV images. Minimum and maximum diameters are observed at instants  $t = 0$  ms ( $k = 0$ ) and  $t = 250$  ms ( $k = 6$ ). Mean and uncertainty values are computed over the 500 PIV images at each observed instant.

## **Appendices figure legends**

### Appendix A:

Table 1: Summary of in vitro arterial flow studies cited in the introduction (and more) with specific features regarding phantom geometries, walls properties, and blood-mimicking fluids.

### Appendix B:

Figure B1: Shear-viscosity follow-up during the experiments. It corresponds to the maximum duration of flow looping and pumping to conduct an experiment along which the xanthan polymer chains could be damaged. Thanks to the Moineau pump system that preserves polymers, viscosity properties appear constant.

Fig B2: Example of wall detection and masking steps for one image. (a) Particles image with enhanced contrasts to highlight the phantom walls, (b) wall detection with thresholding to select walls greyscale values. (c) corresponding generated binary mask for cross-correlation. The definitive masks for each of the 12 imaged instants are mean masks of the 500 images.

Figure B3: Statistical convergence graph of mean velocity per cycle instants “k” (a) in the whole ROI and (b) in an interrogation window (coordinates  $[x_{\text{window}}, y_{\text{window}}] = [70,90]$ ). In the whole ROI, 50 to 100 images are needed to reach statistical convergence. In an interrogation window, from 200 to 400 images are needed depending on the cycle instant.

Figure B4: Newtonian and non-Newtonian flowrate and pressure conditions. Lines represent mean values calculated along the 6000 successive cycles of the PIV imaging process for each fluid flow experiment. Error bars correspond to the standard deviation at each point along the 6000 cycles (cycle-to-cycle reproducibility). Data were recorded every 20 ms. The cardiac cycle duration is  $T = 800$  ms.

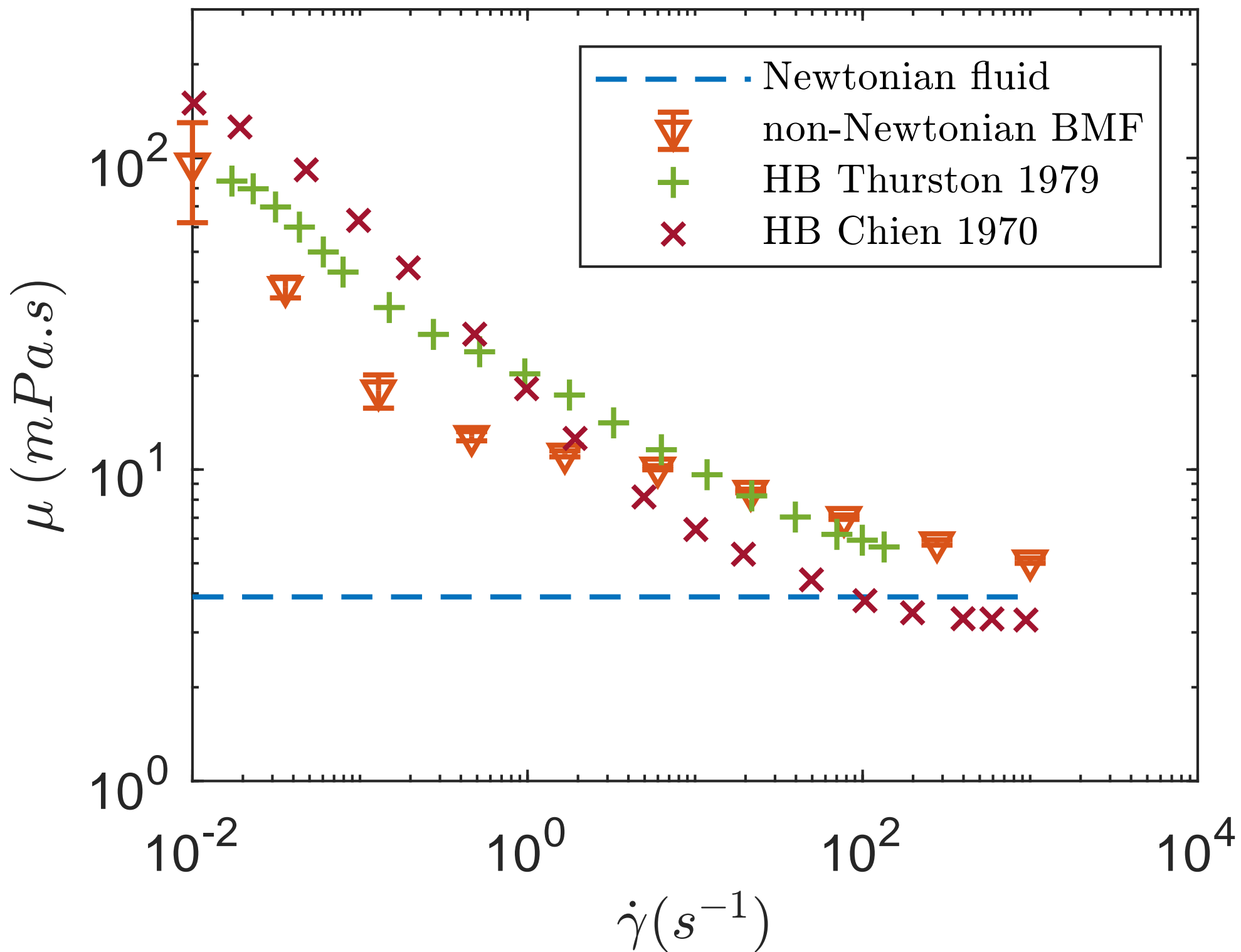
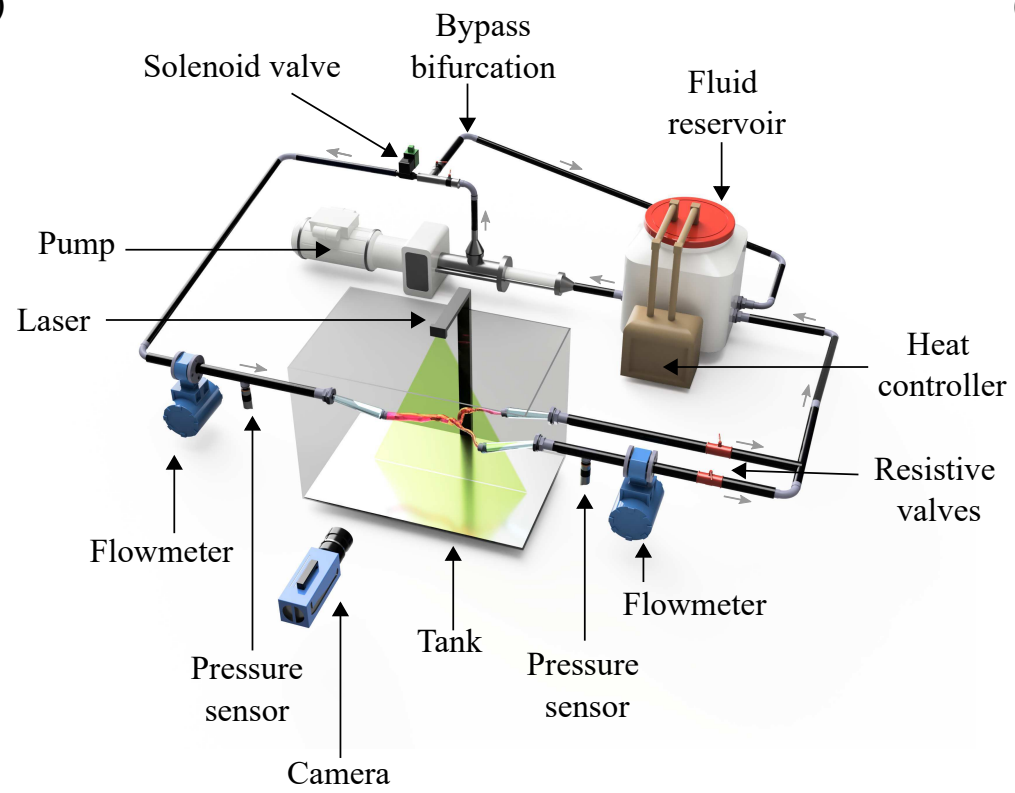


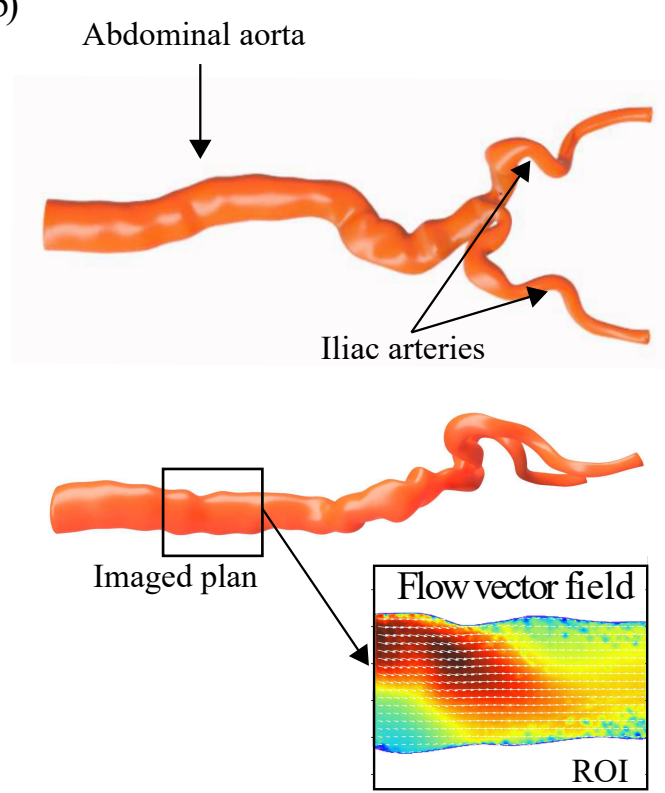
Figure 2 (two column)

[Click here to access/download;Figure;figure2.eps](#)

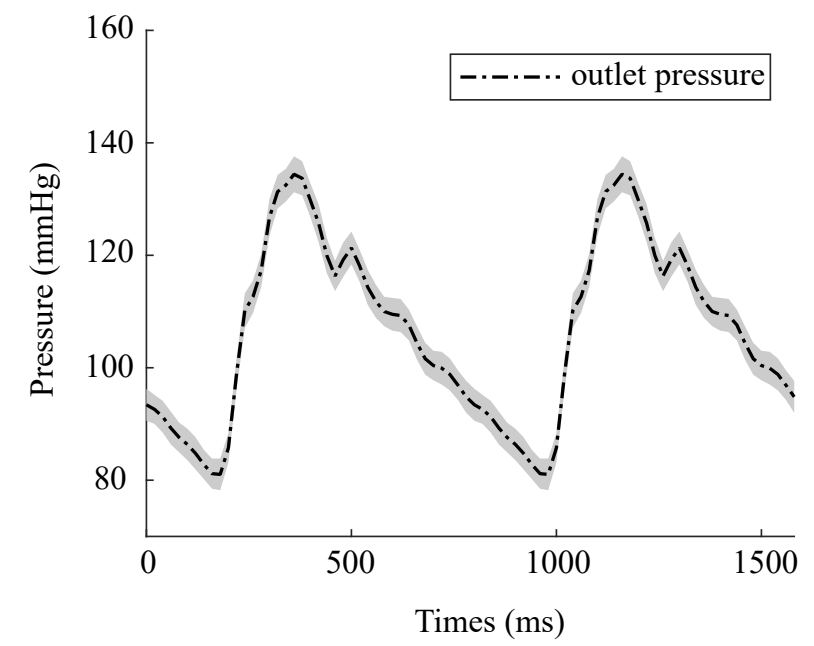
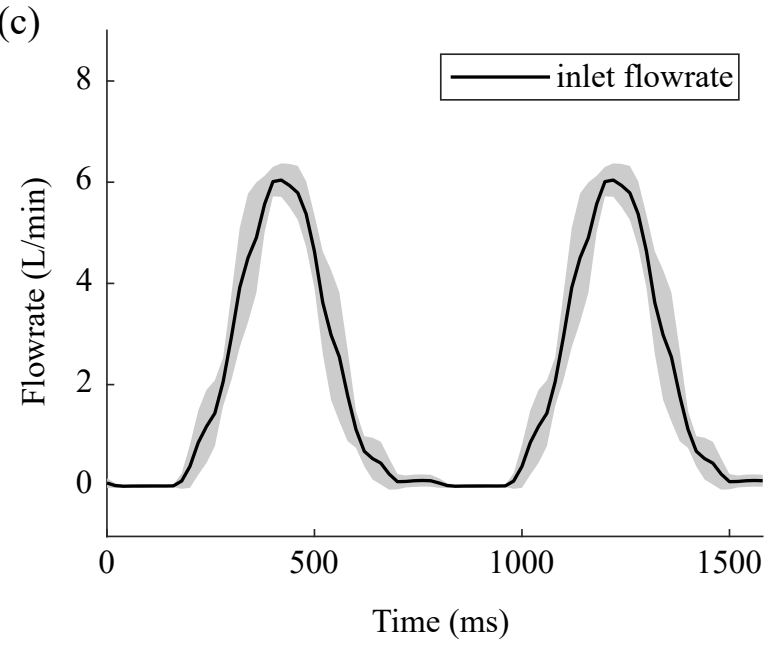
(a)

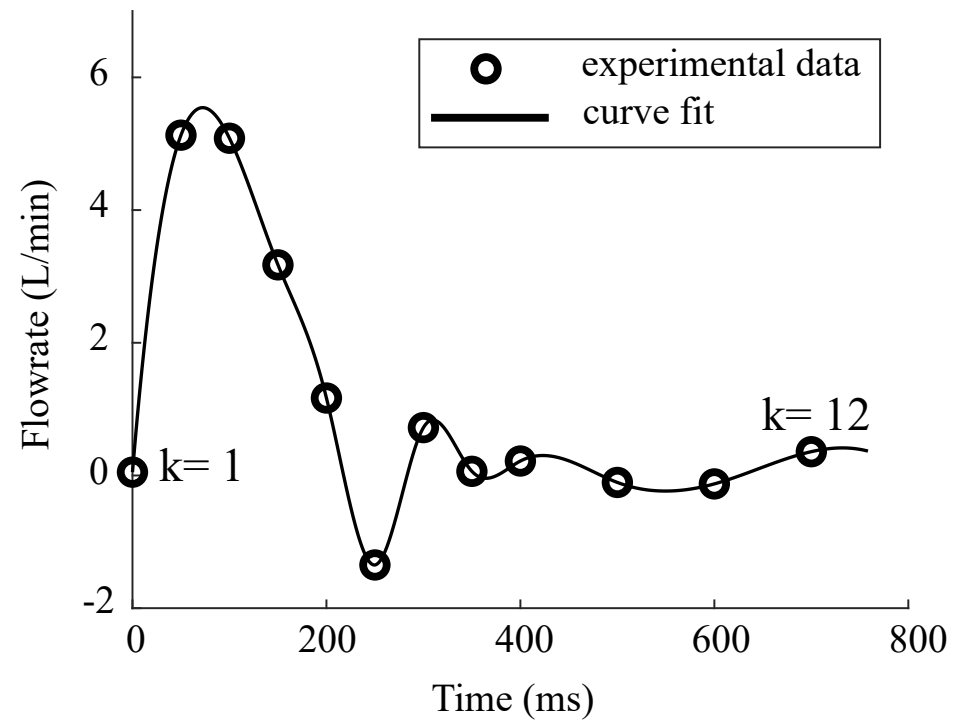


(b)

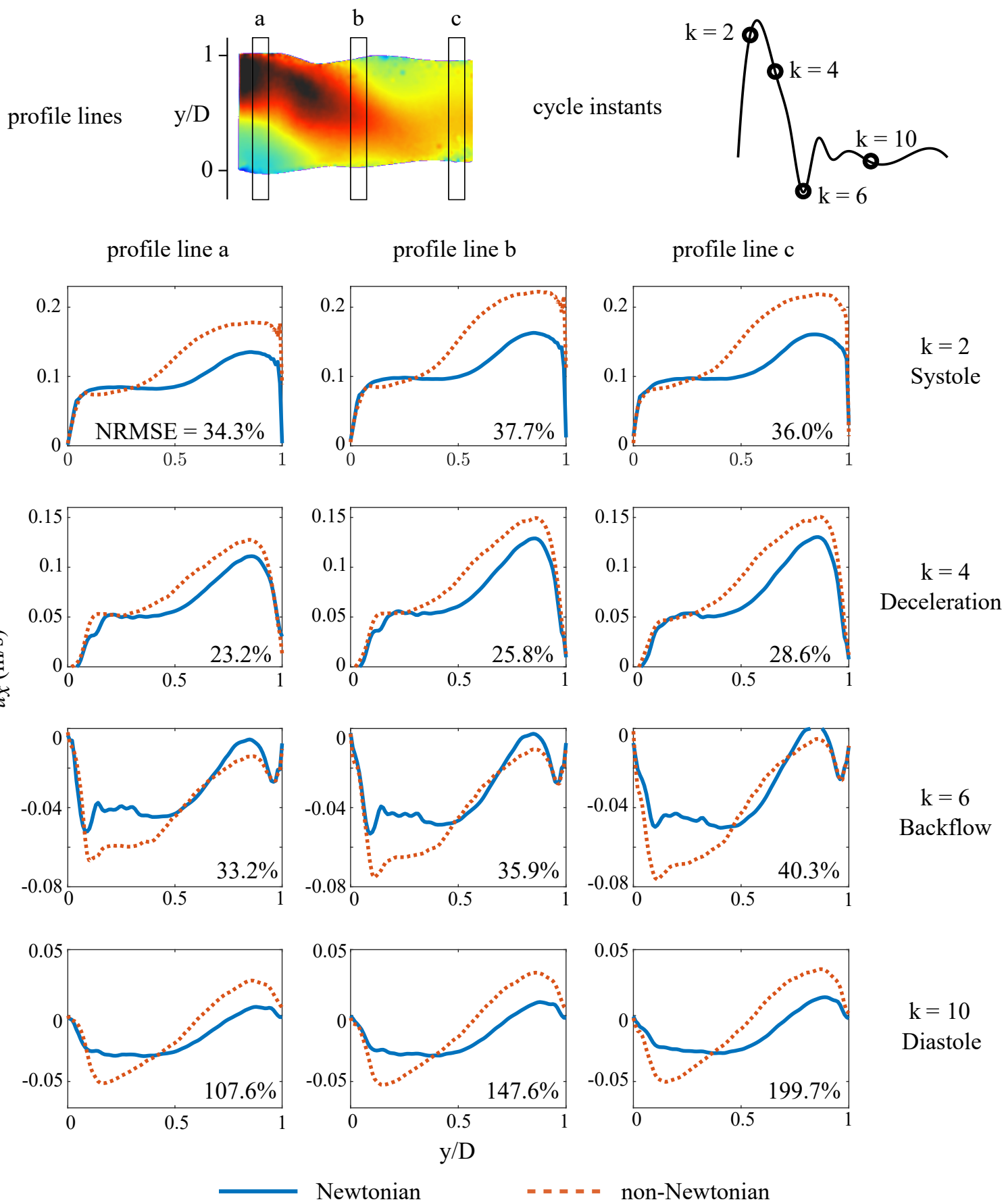


(c)





<b>Cycle instant “k”</b>	<b>1</b>	<b>2</b>	<b>3</b>	<b>4</b>	<b>5</b>	<b>6</b>	<b>7</b>	<b>8</b>	<b>9</b>	<b>10</b>	<b>11</b>	<b>12</b>
<b>Cycle time (ms)</b>	0	50	100	150	200	250	300	350	400	500	600	700
<b><math>\Delta t</math> (ms)</b>	5	3	3	3	3	4	5	6	6	7	8	4
<b>Number of acquired images/cycles</b>	500	500	500	500	500	500	500	500	500	500	500	500
<b>Total number of acquired cycle/images</b>	6000											



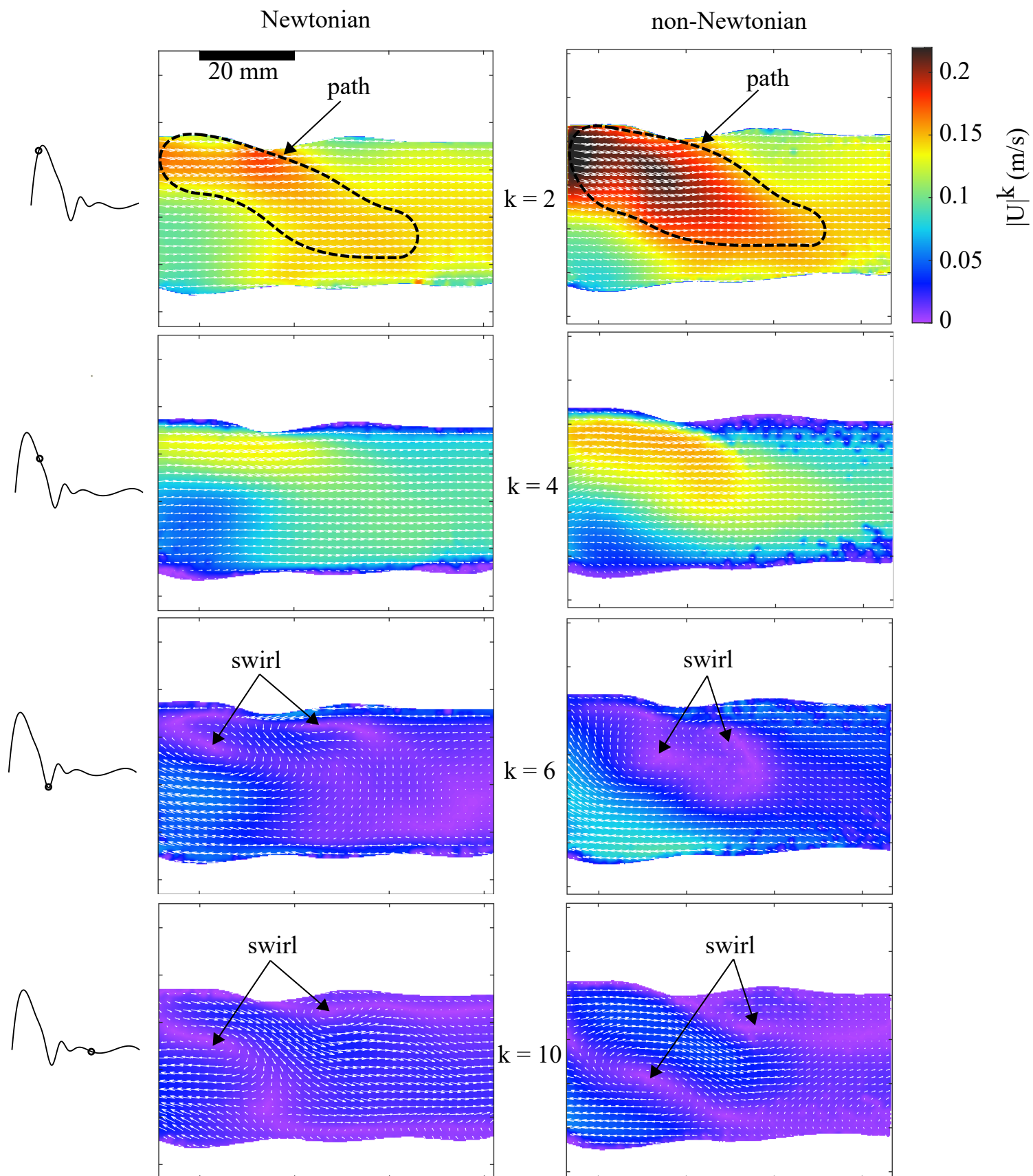
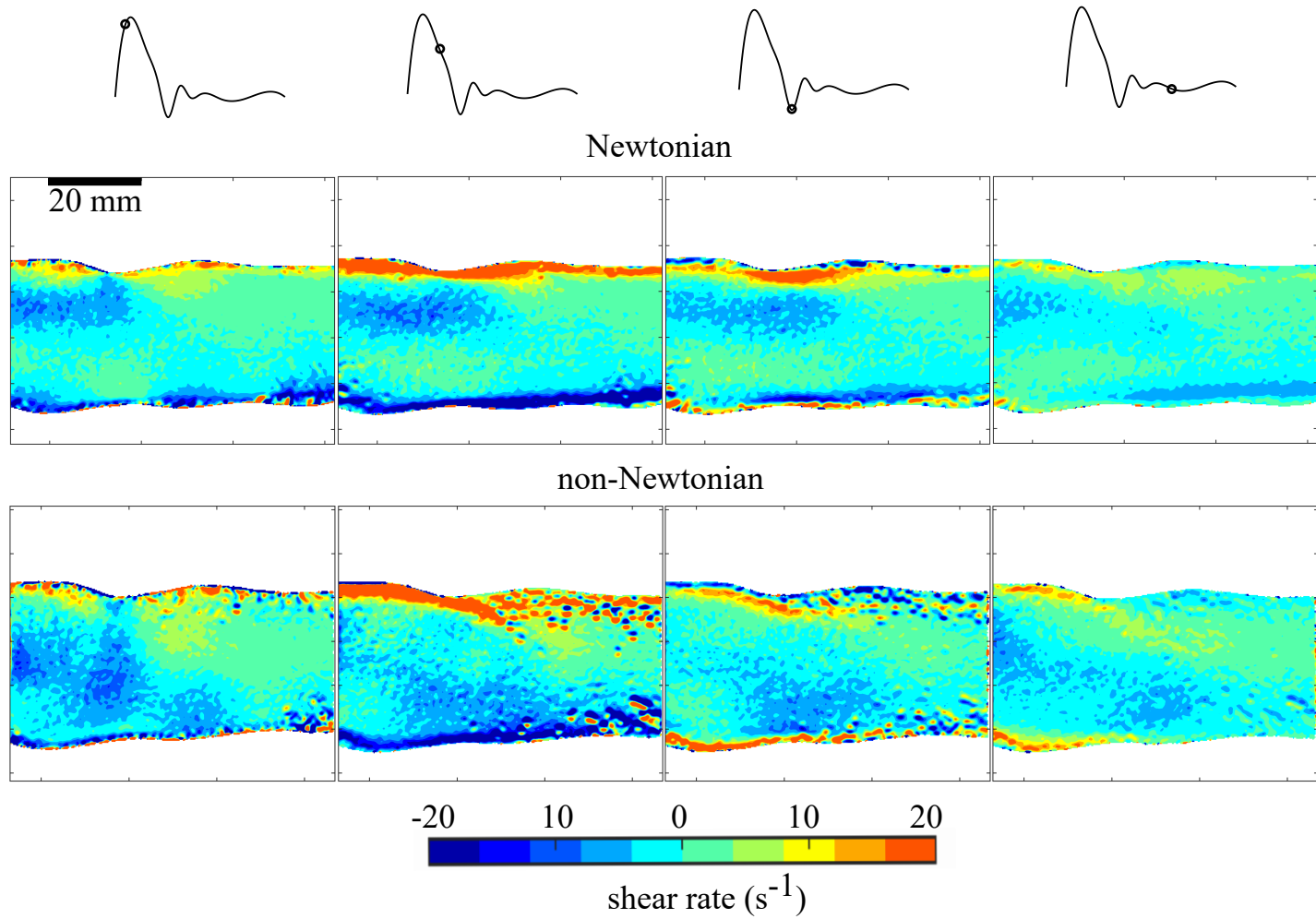
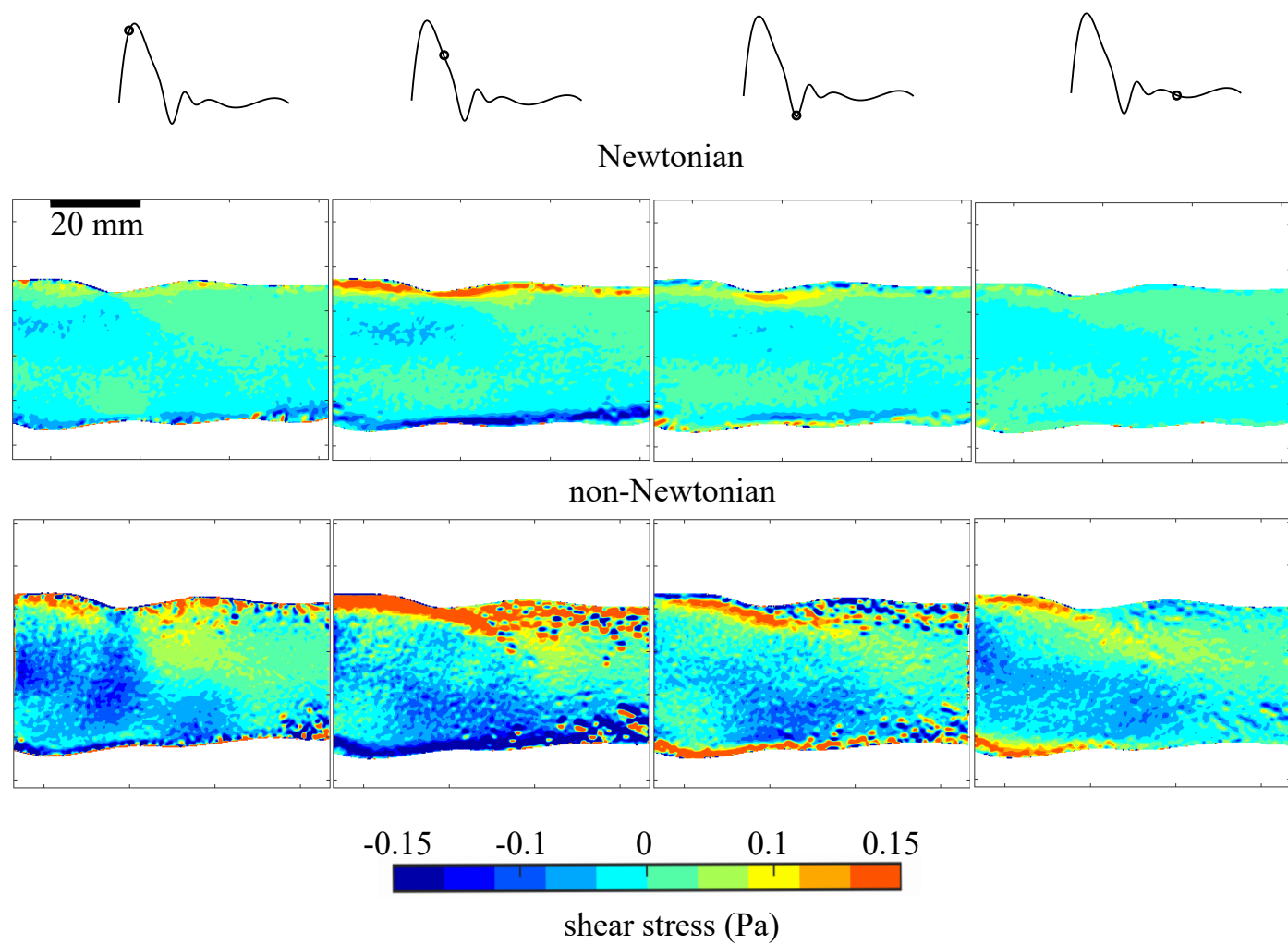


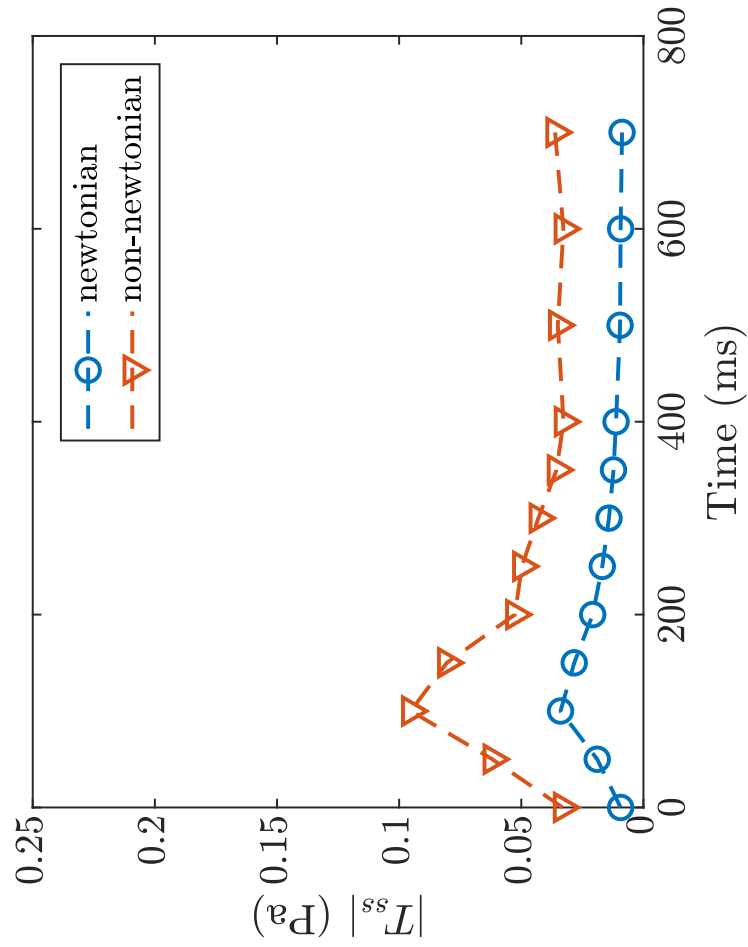
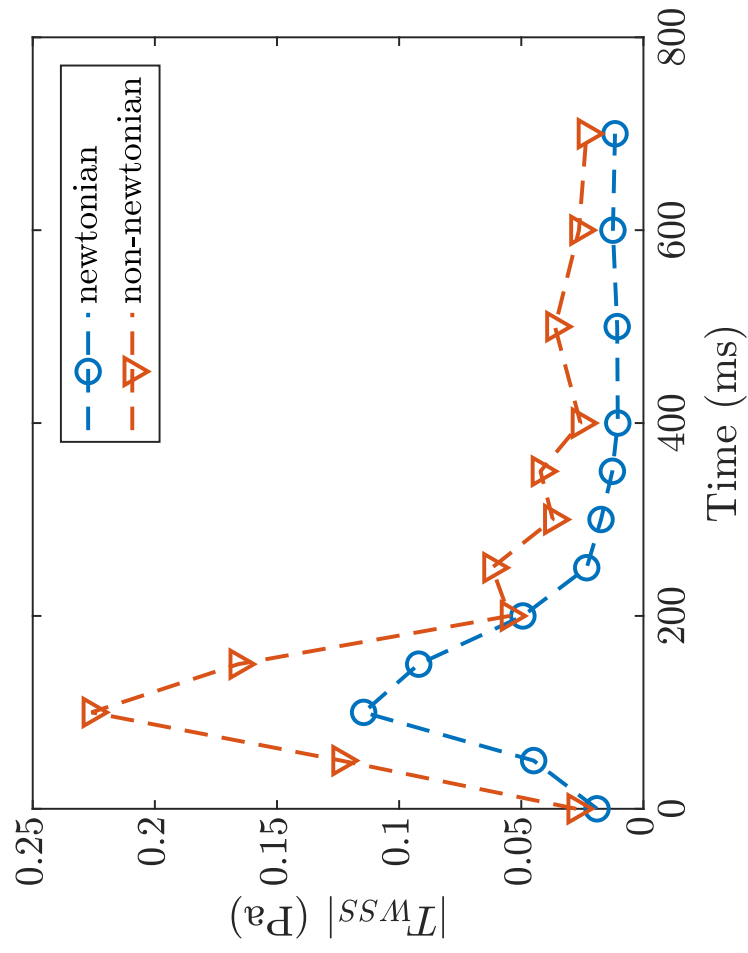
Figure 6 (two column)  
(a)

[Click here to access/download;Figure;figure6.eps](#)



(b)





**Tables**

Fluid flow	Mean error (m/s)	Maximum error (m/s)
Newtonian	$7.10^{-4}$	$5.10^{-3}$
Non-Newtonian	$8.10^{-4}$	$4.10^{-3}$

Table 1: Mean and maximum uncertainties computed on the whole set of PIV images. Maximum error corresponds to the worst case error in the interrogation windows. For each cycle instant, the error was computed with the Type A uncertainty method (JCGM, 2008) for all the interrogation windows of the 12 velocity fields ( $n = 500$  data for each field). The mean error is the mean uncertainty on of all the interrogation windows of the 12 cycle instants. The maximum error is the worst uncertainty found in an interrogation window.

	Newtonian	Non-Newtonian	Difference
Density, $\rho$ [ $\text{kg}\cdot\text{m}^{-3}$ ]	1146	1146	2.37 %
Viscosity, $\mu$ [ $\text{mPa}\cdot\text{s}$ ]	3.9	5.2	33.3 %
<b>Flow conditions</b>			
Mean inlet flowrate, $Q_{\text{in mean}}$ [L/min]	$1.69 \pm 0.44$	$1.73 \pm 0.44$	2.37 %
Maximum inlet flowrate, $Q_{\text{in max}}$ [L/min]	$5.57 \pm 0.30$	$5.80 \pm 0.37$	3.96%
Min outlet pressure, $P_{\text{out min}}$ [mmHg]	$89.58 \pm 2.40$	$90.12 \pm 2.67$	0.60%
Max outlet pressure, $P_{\text{out max}}$ [mmHg]	$139.46 \pm 2.87$	$139.23 \pm 3.60$	0.16 %
Peak Reynolds number, $Re_{\text{peak}}$	$1200 \pm 2$	$1129 \pm 2$	6.2 %
Womersley number, $\alpha$	15.3	14.6	4.8 %

Table 2: Newtonian and non-Newtonian flow experiments parameters. Reynolds and Womersley numbers were calculated with equivalent viscosity at high shear rate for the non-Newtonian case. The peak Reynolds number was calculated with systolic peak diameter and velocity data. Data are provided with their standard deviations computed over the 6000 cycles.

	Newtonian (n = 500)		Non-Newtonian (n = 500)	
	Mean (mm)	Standard deviation (mm)	Mean (mm)	Standard deviation (mm)
Minimum diameter (D0)	31.03	0.04	34.21	0.06
Maximum diameter	31.95	0.06	35.42	0.09
$\Delta D$ along cycle	0.92	0.10	1.20	0.15

Table 3: Diameter change with mean and standard deviation values based on diameter computation with PIV images. Minimum and maximum diameters are observed at instants  $t = 0$  ms ( $k = 0$ ) and  $t = 250$  ms ( $k = 6$ ). Mean and uncertainty values are computed over the 500 PIV images at each observed instant.

**Appendices**

Appendix A:

<b>Newtonian BMF</b>		
<b>Geometry/Walls</b>	<b>Rigid</b>	<b>Compliant</b>
<b>Idealized - Standardized</b>	Deplano et al., 2007 Walker et al., 2014 Najjari et al., 2018	Deplano et al., 2007 Kung et al., 2011 Deplano et al., 2014 Najjari et al., 2018
<b>Anatomical</b>	Stamatopoulos et al., 2011 Schirmer and Malek, 2007 Bonfanti et al., 2020 Franzetti et al., 2021 Zimmermann et al., 2021	Gülen et al., 2012 Büsen et al., 2017 Thirugnanasambandam et al., 2021 Zimmermann et al., 2021
<b>Non-Newtonian BMF</b>		
<b>Geometry/Walls</b>	<b>Rigid</b>	<b>Compliant</b>
<b>Idealized - Standardized</b>	Gijsen et al., 1998 Schirmer and Malek, 2007 Anastasiou et al. 2011 Walker et al., 2014 Najjari et al., 2016b	Deplano et al., 2014 Deplano et al., 2016
<b>Anatomical</b>	x	x

Table A1: Summary of in vitro arterial flow studies cited in the introduction (and more) with specific features regarding phantom geometries, walls properties, and blood-mimicking fluids.

## Appendix B:

Four supplementary figures are provided in the appendix (figure B1, B2, B3, and B4). The aorta 3D model and two PIV maps animations (images post-treatment overview and shear stress) are also accessible as complementary materials.

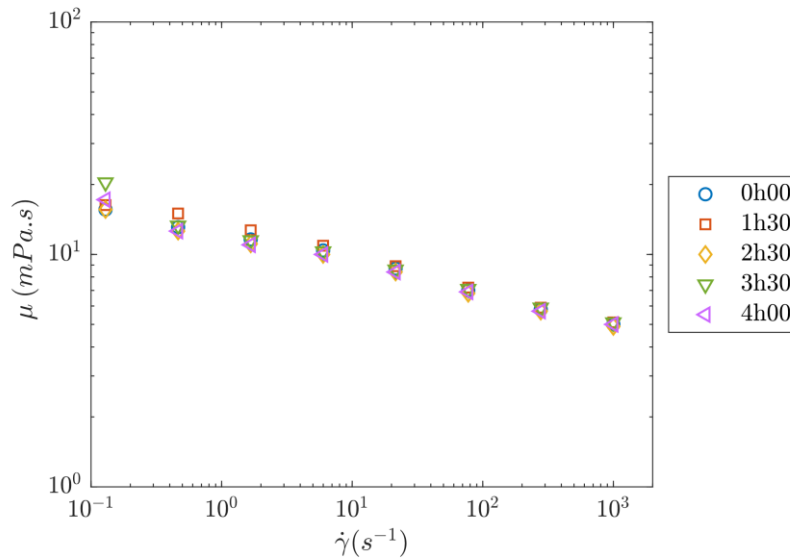


Figure B1: Shear-viscosity follow-up during the experiments. It corresponds to the maximum duration of flow looping and pumping to conduct an experiment along which the xanthan polymer chains could be damaged. Thanks to the Moineau pump system that preserves polymers, viscosity properties appear constant.

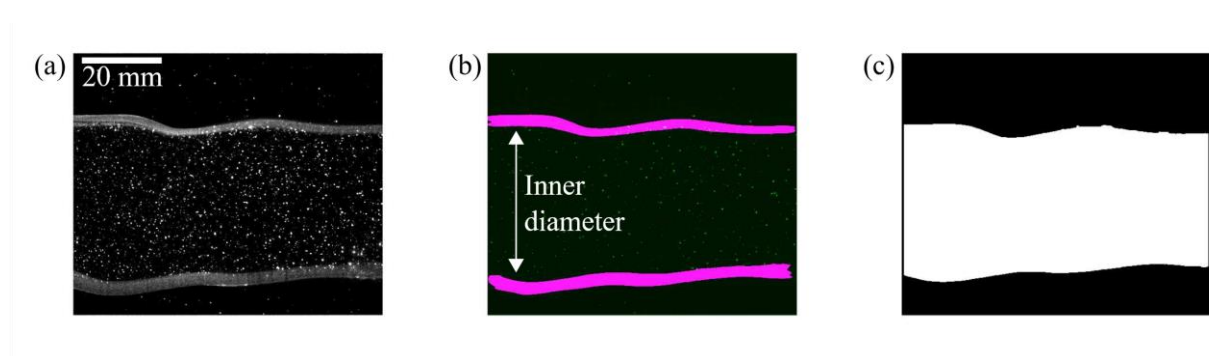


Fig B2: Example of wall detection and masking steps for one image. (a) Particles image with enhanced contrasts to highlight the phantom walls, (b) wall detection with thresholding to select walls greyscale values. (c) corresponding generated binary mask for cross-correlation. The definitive masks for each of the 12 imaged instants are mean masks of the 500 images.

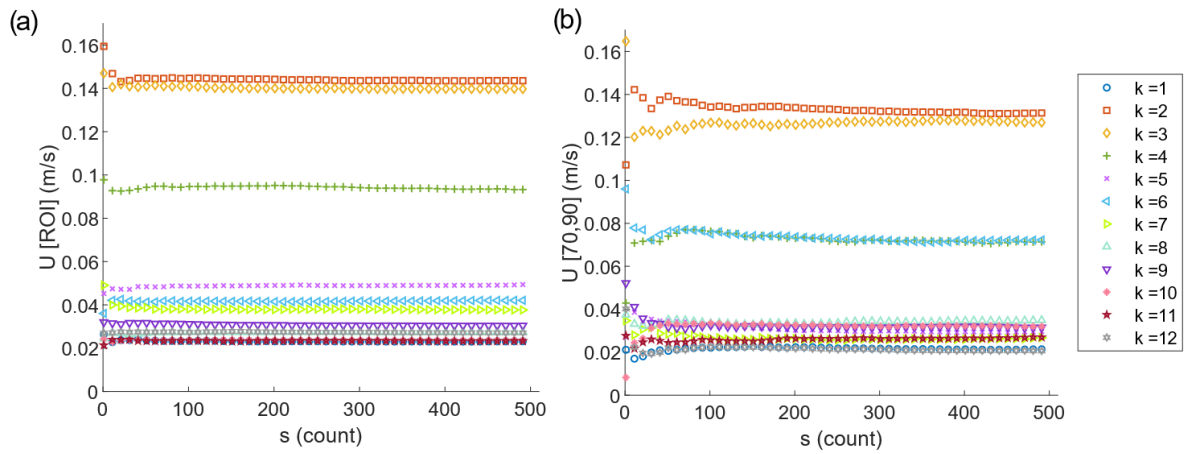


Figure B3: Statistical convergence graph of mean velocity per cycle instants “k” (a) in the whole ROI and (b) in an interrogation window (coordinates  $[x_{\text{window}}; y_{\text{window}}] = [70,90]$ ). In the whole ROI, 50 to 100 images are needed to reach statistical convergence. In an interrogation window, from 200 to 400 images are needed depending on the cycle instant.

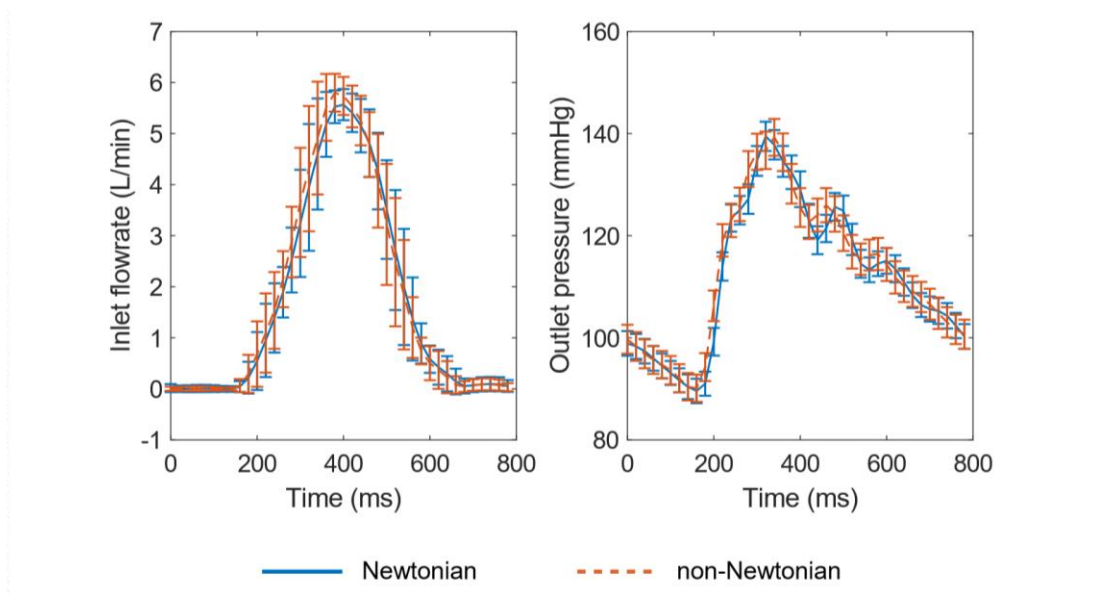


Figure B4: Newtonian and non-Newtonian flowrate and pressure conditions. Lines represent mean values calculated along the 6000 successive cycles of the PIV imaging process for each fluid flow experiment. Error bars correspond to the standard deviation at each point along the 6000 cycles (cycle-to-cycle reproducibility). Data were recorded every 20 ms. The cardiac cycle duration is  $T = 800$  ms.